Femtosecond dynamics of solvated oxygen anions. I. Bifurcated electron transfer dynamics probed by photoelectron spectroscopy

D. Hern Paik, Nam Joon Kim, and Ahmed H. Zewail

Citation: The Journal of Chemical Physics **118**, 6923 (2003); doi: 10.1063/1.1561433
View online: http://dx.doi.org/10.1063/1.1561433
View Table of Contents: http://scitation.aip.org/content/aip/journal/jcp/118/15?ver=pdfcov
Published by the AIP Publishing

Femtosecond dynamics of solvated oxygen anions. I. Bifurcated electron transfer dynamics probed by photoelectron spectroscopy

D. Hern Paik, Nam Joon Kim, and Ahmed H. Zewail[a)]
Arthur Amos Noyes Laboratory of Chemical Physics, Laboratory for Molecular Sciences, California Institute of Technology, Pasadena, California 91125

(Received 10 October 2002; accepted 23 January 2003)

The ultrafast dissociation dynamics of $O_6^- \cdot X$ ($X = O_2$, N_2, Xe, or N_2O) was investigated by femtosecond photoelectron spectroscopy. The transients, monitoring nascent O_2^-, exhibit biexponential rises with two distinct time constants—the fast component ($\tau_1 \sim 200$ fs) corresponds to the joint rate constant for electron recombination and direct dissociation of the O_4^- core perturbed by solvent molecules, whereas the slow component ($\tau_2 = 2.0-7.7$ ps, depending on the solvent) corresponds to the process for the liberation of O_2^-, which is governed by vibrational predissociation and intramolecular vibrational-energy redistribution. These observations are consistent with the mechanism proposed in the earlier communication of this work [Paik *et al.*, J. Chem. Phys. **115**, 612 (2001)]. The wave packet bifurcates via two separate dissociation pathways: electron transfer followed by electron recombination, and electron transfer followed by vibrational predissociation. Unlike all other solvents, the anomalous behavior observed for $O_6^- \cdot N_2O$—a threefold increase in τ_2 value, compared to the other solvents, and a factor of 10 increase for τ_2, compared to that of O_6^-—reflects the more effective energy dissipation via solute–solvent vibration-to-vibration and rotational couplings. Moreover, for all solvents, the ratio of the slow-rise contribution to the total signal can be correlated with the degree of cooling, supporting the concept of bifurcation in the two channels. © *2003 American Institute of Physics.*
[DOI: 10.1063/1.1561433]

I. INTRODUCTION

Studies of size-selected clusters provide valuable insights on the nature of solute–solvent interactions, with the hope of bridging the gap between the isolated gas-phase and condense-phase dynamics. These microscopic solvation processes, which may involve energy redistribution, electron transfer, and vibrational predissociation, have been examined in a variety of ionic[1–9] and neutral[10–14] clusters.

In an earlier communication,[9] we reported on studies of O_2^- clusters, and in this paper we give a full account of the study and extend the scope to include clusters of O_6^- with a variety of solvents, $X = O_2$, N_2, Xe, or N_2O. Specifically, we report on the femtosecond (fs) time-resolved photoelectron (PE) spectra. The number of solvent molecules studied here is always one while in the accompanying paper the O_2 solvent composition varies from 3 to 10. These clusters are unique for a number of reasons: First, the O_6^- cluster is composed of the O_4^- core surrounded by a neutral O_2 molecule. Second, upon irradiation with a 800 nm fs pulse, the electron migrates from the O_4^- core to the neutral O_2 molecule; subsequently, an O_2^- fragment is generated via two different channels, as discussed in Ref. 9. The solvent, N_2, Xe, or N_2O is weakly bound to the O_4^- core and not directly involved in an electron migration process, as evidenced from the photoelectron spectra and the nascent fragments produced. Finally, for these clusters we can follow the change of the PE spectra with time.

In the present work, we examine the effect of the solvent on the observed rise of O_2^- and the change of the photoelectron spectra of $O_6^- \cdot X$. We consider the bifurcation of the initial wave packet to produce O_2^- in two channels and we compare the observed rates to calculations based on the statistical (RRKM) theory for the dissociation of $O_6^- \cdot X$, through vibrational-energy redistribution, and the prompt dissociation through back-electron transfer. A strong solvent dependence was evident in both the rates and the contribution of population in both channels.

II. EXPERIMENT

Our molecular beam apparatus consists of a negative ion source, a linear reflectron[15] time-of-flight (TOF) mass spectrometer and a ''magnetic-bottle'' [16] photoelectron spectrometer. A schematic of the apparatus is shown in Fig. 1.

Negative ions were produced by a pulsed electron impact source. The pulsed supersonic expansion was crossed with 1.0 keV electron pulse (1.0 ms), and anions were produced by the secondary electron attachment. The ions passing through the skimmer (1.5 mm hole) were then accelerated to the field-free region by applying electric pulse (-2.0 kV) to the two-stage repeller.[17] The electric potential of the second stage repeller is adjusted so that the focus along the time-of-flight axis of the ion bunches is at the laser interaction region. The ions spatial distribution (perpendicular to the time-of-flight axis) was focused at the center hole of the MCP using an Einzel lens. A set of horizontal and vertical deflection plates were used to steer the ion beam.

a)Electronic mail: zewail@caltech.edu

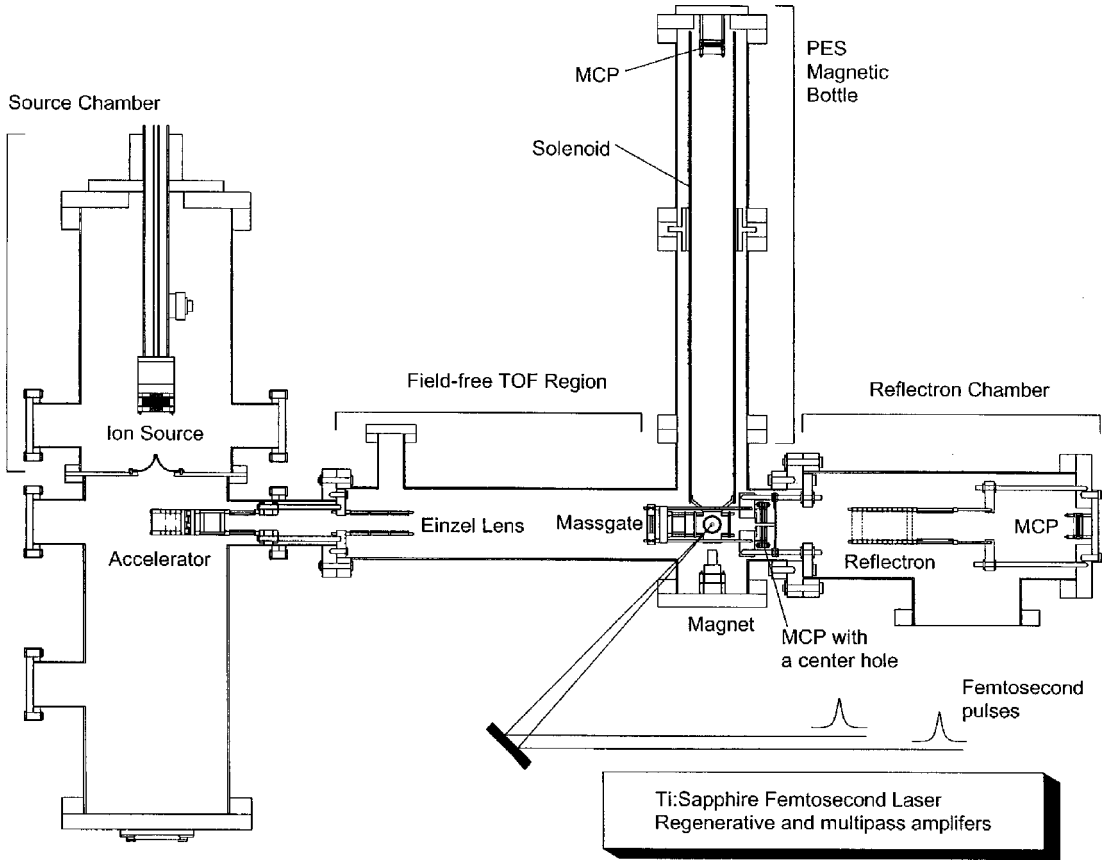

FIG. 1. Schematic of molecular beam—femtosecond laser apparatus.

In the field-free region, the ion bunches were separated by their masses, and the mass of interest was selected by the interleaved-comb mass gate[18] that provides a mass selection, by applying a high electric field (1.0 kV/1.0 mm) between two alternating wires. After mass selection, the ion bunch was intercepted with the femtosecond laser pulses, and the photoelectrons were collected by the magnetic bottle photoelectron spectrometer. The photofragments were detected by the linear reflectron time-of-flight mass spectrometer.

Femtosecond laser pulses (110 fs, 800 nm) were generated from a Ti:sapphire oscillator that was optically pumped by the second harmonic (532 nm) of a cw Nd:YAG laser. The oscillator output was then amplified by the regenerative and multipass amplifiers. The amplified 800 nm light (20 Hz) was frequency doubled by a BBO crystal to generate 800 μJ of the 400 nm light. The remaining 800 nm output (1.5 mJ) was used as the pump pulse for photodissociating $O_6^- \cdot X$ clusters, while the 400 nm laser pulse was used as probe for photodetaching nascent anionic fragments. Black anodized light baffles were installed in order to reduce the background noise generated from the scattered light. In order to prevent multiphoton processes while maximizing the overlap between the laser pulse and ion beam, the laser beam waist was collimated only to 5 mm diameter. We also studied the power dependency (see Paper II).

The $O_6^- \cdot X$ ($X=N_2$, Xe, or N_2O) anionic clusters were generated by crossing the electrons (1 keV) with the gas mixture of approximately 90% of oxygen and 10% of solvents (N_2, Xe, or N_2O). The mixing ratio was maintained constant by utilizing mass flow controllers. The residual water trace was removed by passing the gas mixture through a cryotrap of $-50\,^{\circ}C$.

III. RESULTS

Figure 2 shows the mass spectra of $O_6^- \cdot X$ ($X=N_2$, Xe, or N_2O) recorded under the optimal ion-source conditions for generating $O_6^- \cdot X$. In the figure we show the clusters formed under our expansion conditions. The dominance of O_4^- and $O_4^- \cdot X$ indicates that the solvent is attached to the O_4^- core. Similar to our previous observation with O_6^-[9] and higher clusters,[19] upon irradiation by a 800 nm fs pulse, the $O_6^- \cdot X$ clusters produced the O_2^- fragment, whereas $O_4^- \cdot X_n$ ($n=1,2$; $X=N_2$, Xe or N_2O) did not generate any negatively charged fragment. This suggests that $O_4^- \cdot O_2$, not $O_4^- \cdot X$, is the essential chromophore for the interaction with the 800 nm pulse. We did not observe the O_4^- fragment when the 800 nm pulse was used to excite $O_6^- \cdot X$ ($X=N_2$, Xe or N_2O); for $O_6^- \cdot O_2$, a small amount of the O_4^- fragment was observed. The broad peaks of $O_4^- \cdot Xe$ and $O_6^- \cdot Xe$ are due to the presence of $^{128-136}Xe$ isotopes. In our experiment, $O_6^- \cdot {}^{132}Xe$ was selectively intercepted with the laser pulse in order to avoid irradiating O_{14}^- whose mass is identical to $O_6^- \cdot {}^{128}Xe$. This selection was verified by monitoring the depletion of the $O_6^- \cdot {}^{132}Xe$ ion intensity in the reflectron time-of-flight mass spectrometer (not shown). Moreover, the

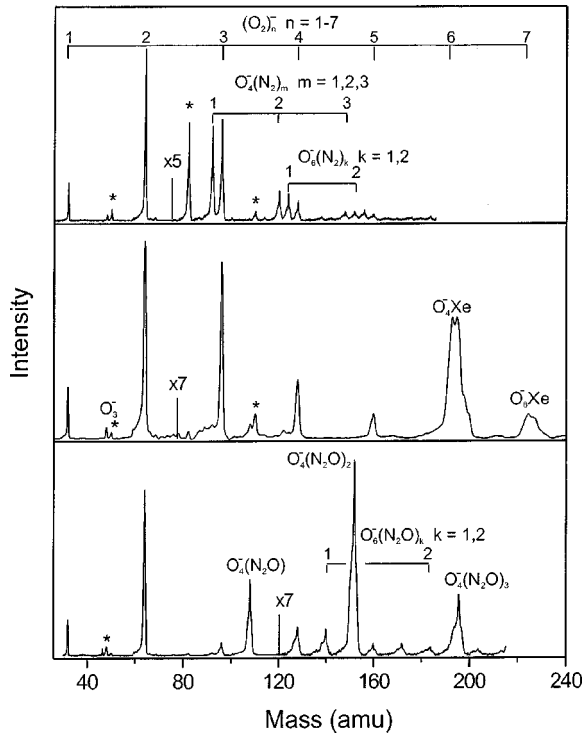

FIG. 2. Time-of-flight mass spectra of $(O_2)_n^- \cdot (X)_m$ ($X=N_2$, Xe, or N_2O) produced by electron impact source, under the optimized condition for the $O_6^- \cdot X$ ($X=N_2$, Xe, or N_2O) generation. The traces of $O_6^- \cdot (H_2O)_m$ clusters are indicated by asterisks.

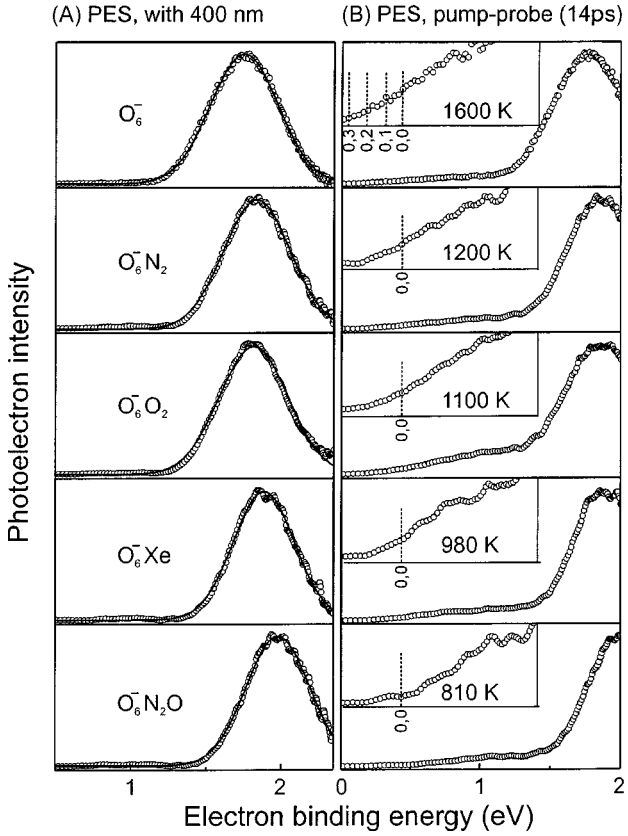

FIG. 3. (a) Photoelectron spectra of $O_6^- \cdot X$ ($X=O_2$, N_2, Xe, or N_2O) with probe (400 nm) pulse only. The experimental results (open circles) are fitted to a Gaussian function (solid line) and the peak of the Gaussian function was assigned as the vertical detachment energy. (b) Photoelectron spectra of $O_6^- \cdot X$ ($X=O_2$, N_2, Xe, or N_2O) collected when both the pump (800 nm) and probe (400 nm) pulses were present at a 14 ps delayed time. The photoelectron envelope at lower binding energy is that of the nascent O_2^- fragment, and the higher binding energy peak is due to the parent cluster excited by 400 nm light. The enlarged plots of the nascent O_2^- photoelectron profiles are presented as insets. The positions of hot bands and an 0,0 band are indicated by the vertical lines, and the estimated temperature of O_2^- is given in the inset.

absence of O_{14}^- in the interaction region between the laser and the ion beam was confirmed by comparing the $O_6^- \cdot Xe$ and O_{14}^- transients.[19]

The photoelectron spectra of $O_6^- \cdot X$ at 400 nm (3.1 eV) are shown in Fig. 3(a). The shapes of spectra resemble the photoelectron spectrum of O_6^-, but both the peak [vertical detachment energy (VDE)] and the onset [adiabatic electron affinity (AEA)] are shifted toward higher electron binding energies. The resemblance of the photoelectron profiles suggests that the solvent is attached to O_6^- by a weak interaction without altering its chemical properties. The increase in binding energy corresponds to the stabilization energy by the solvent X. Among the solvent molecules, O_6^- is stabilized most by N_2O and stabilized least by O_2. We note that among the solvents, N_2O is the only one that has a dipole moment. The stabilization energy $[E_{st}=\mathrm{VDE}(O_6^- \cdot X)-\mathrm{VDE}(O_6^-)]$ is listed in Table I, together with the literature values for the dipole and quadrupole moments and polarizabilities.[8,20–23]

Figure 3(b) shows the photoelectron signals of $O_6^- \cdot X$ when the probe (400 nm) arrived 14 ps after the pump (800 nm). The pump/probe photoelectron spectra exhibit two peaks. The new peak (in contrast with a 400 nm pulse only) at lower binding energy corresponds to the photoelectron signal of the nascent O_2^- fragment, which is dissociated from $O_6^- \cdot X$ by the 800 nm pulse. From the observed curve and knowledge of the position of the (0,0) and hot (0,1; 0,2 and 0,3) bands of O_2^-, we can estimate the relative population of the hot bands [see Fig. 3(b) and Ref. 24], and obtain the effective temperature; the Franck–Condon factors were deduced from a Morse potential approximation.[25] The hot band tail was fitted with Gaussian functions with FWHM $=0.17$ eV (our instrument resolution), and from the temperature values, the average internal energy (k_BT) of the nascent O_2^- was deduced.

The onset of O_2^- generated from the dissociation of $O_6^- \cdot X$ are shifted toward a higher electron binding energy, when compared to the onset of O_2^- dissociated from O_6^-. The observed shift in Fig. 3(b) reflects the cooling of the nascent O_2^- fragment from parent $O_6^- \cdot X$. The degree of cooling varies with clusters $O_6^- \cdot X$ ($X=O_2$, N_2, Xe, or N_2O), as evident by the trend. This behavior is schematically illustrated in Fig. 4, and the estimated temperatures are given in Table I. Figure 4 emphasizes the sensitivity of photoelectron spectra to changes in binding and temperature of the nascent O_2^- product.

Figure 5 shows the femtosecond transients of O_2^- generated from the $O_6^- \cdot X$ dissociation. The transients were recorded by integrating the photoelectron signal of O_2^- [see Fig. 3(b)] at different time delays between pump and probe pulses. They exhibit biexponential rises with two distinct

TABLE I. Summary of experimental results, RRKM calculations, and literature values of dipole and quadrupole moments and polarizabilities.

	Experimental results					RRKM	Literature values[b]			
Solvent	E_{st} (eV)	T (K)	γ	τ_1 (fs)	τ_2 (ps)	τ_2 (ps)	μ^a (D)	Θ^a (esu cgs)	α^a (a.u.)
None	···	1600	4.0	110	0.7	···	···	···	···
N_2	0.08	1200	3.7	200	2.0	1.6	0	-14.7×10^{-27}	11.82
O_2	0.06	1100	2.7	230	2.4	1.6	0	-4.0×10^{-27}	10.95
Xe	0.12	980	1.9	190	2.1	1.1	0	···	27.11
N_2O	0.23	810	1.3	235	7.7	4.5	0.16	-3.36×10^{-26}	20.35

[a]μ, Θ, and α refer to the dipole moment, quadrupole moment, and polarizability, respectively.
[b]References are indicated in the parentheses: quadrupole moments and polarizabilities of N_2 and O_2 (8); polarizability of Xe (20); dipole moment (21), quadrupole moment (22) and polarizability (23) of N_2O.

time constants for all clusters, but the time constants and amplitude ratios vary depending on the solvent. The time constants (τ_1 and τ_2) and the amplitude ratios ($\gamma \equiv A_1/A_2$) were obtained by fitting the transient data with a biexponential growth function, and the values are tabulated in Table I. In this treatment, the response function was included using the autocorrelation function of our pulse width (110 fs) at 800 nm, however, we also checked for the values of the fit without convolution and obtained similar values for τ_1, τ_2, and γ, except for the 200 fs component, which without convolution becomes somewhat longer. These experiments were repeated many times, and all show the same general trend: the slow component increases in contribution, and its time constant increases as the solvent was changed from N_2 to N_2O, with O_2 and Xe being in the middle. In Fig. 6, we plot the changes in τ_2 for these different solvents and the dependence on cooling, as discussed below.

IV. DISCUSSION

From the above results we conclude that the dynamics of solvated O_6^- follows the same energy landscape as in the case of bare O_6^-—a bifurcation of the wave packet motion in two different channels. Upon excitation at 800 nm, the electron in $O_4^- \cdot O_2$ migrates from the core to the solvent forming the $O_4 \cdot O_2^-$ complex; subsequently, $O_4 \cdot O_2^-$ dissociates via two different channels with distinct time constants. The fast component ($\tau_1 = 110$ fs) represents the direct dissociation, following electron recombination (ER) of the O_4^- core on a repulsive potential surface. The slow component ($\tau_2 = 700$ fs) involves intramolecular vibrational-energy redistribution (IVR)/vibrational predissociation (VP) to liberate the negatively charged O_2^- solvent molecule from the charge transferred $O_4 \cdot O_2^-$ complex. The two steps can be written as follows:

$$O_4^- \cdot O_2 + h\nu \rightarrow O_4 \cdot O_2^{-*\ddagger} \xrightarrow{\text{direct (ER)}} O_2^- + 2O_2 \quad (1a)$$

$$\xrightarrow{\text{indirect (IVR/VP)}} O_2^- + 2O_2 \quad (1b)$$

The solvation of O_6^- by O_2, N_2, Xe, or N_2O does not form a new chemical species, as discussed above. Accordingly, the same mechanism holds for the motion of the wave packet represented on the potential energy curves in Fig. 7. The upper panel shows the S_N2-type reaction, while the middle panel depicts the two channels described by Eqs. (1). The wave packet preparation and its subsequent bifurcation on the two different potential energy surfaces (direct and indirect) are on different time scales: femtosecond (fs) and

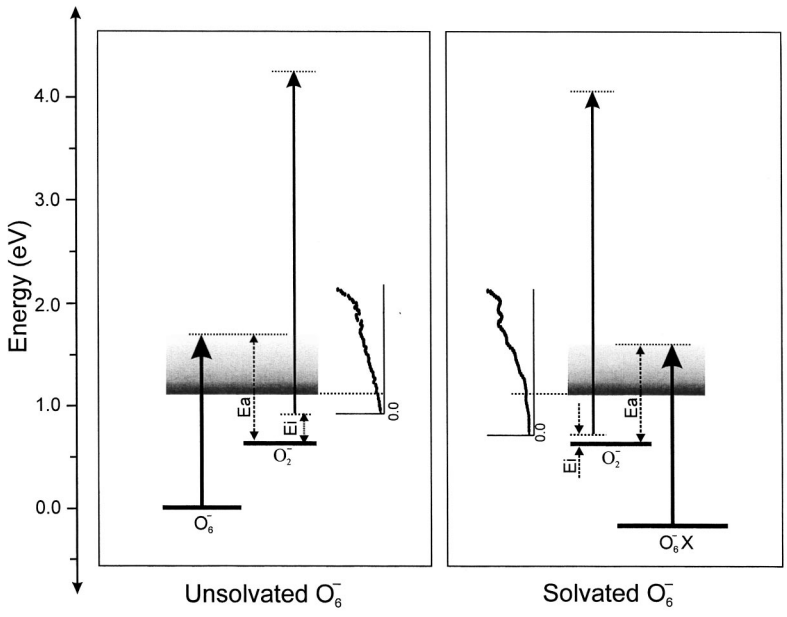

FIG. 4. Energetics of electron detachment. The left-hand panel shows the PE spectrum of O_2^- fragment dissociated from unsolvated O_6^-, whereas the right-hand panel shows the PE spectrum of an O_2^- fragment dissociated from solvated ones. The thick and thin vertical arrows represent the pump (800 nm) and probe (400 nm) photon energy, and the photoelectron spectra are shown on the vertical axes. E_i is the internal energy of O_2^- fragment, and E_a is the available energy acquired from the 800 nm pump pulse. E_a in O_6^- is larger than E_a of the solvated one because of the stabilization energy. The ground state of $O_6^- \cdot X$ is shifted downward with respect to O_6^- due to the stabilization energy by X. Notice that the origin (i.e., zero electron binding energy) of the spectrum is shifted relative to each other. The origin of O_2^- dissociated from O_6^- is shifted upward with respect to the O_2^- generated from $O_6^- \cdot X$ due to the difference in O_2^- internal energy.

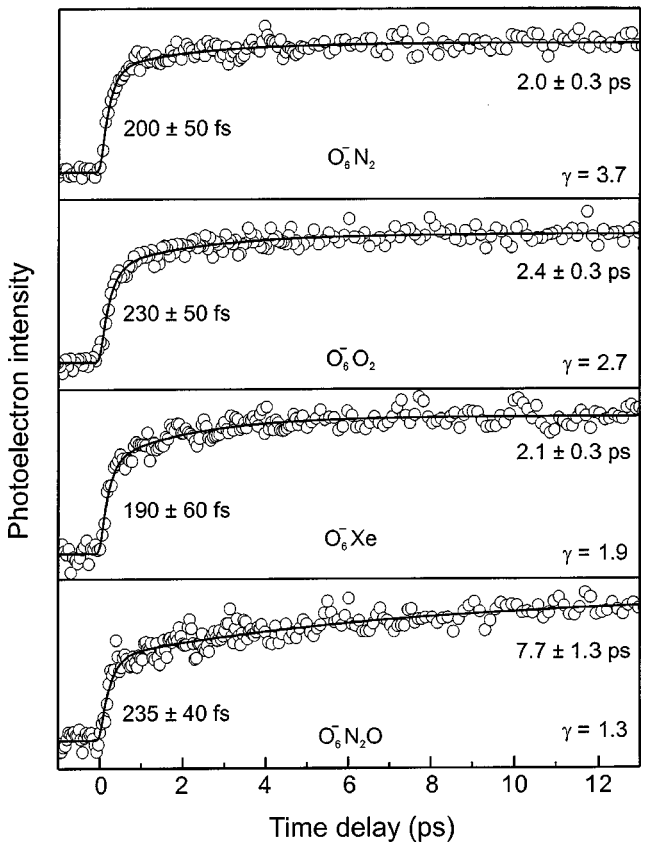

FIG. 5. Femtosecond time-resolved transients of O_2^- rise generated from the dissociation of $O_6^- \cdot X$ ($X=O_2$, N_2, Xe, or N_2O). The time-dependent signals (open circle) were fitted to a biexponential function (solid line); see the text.

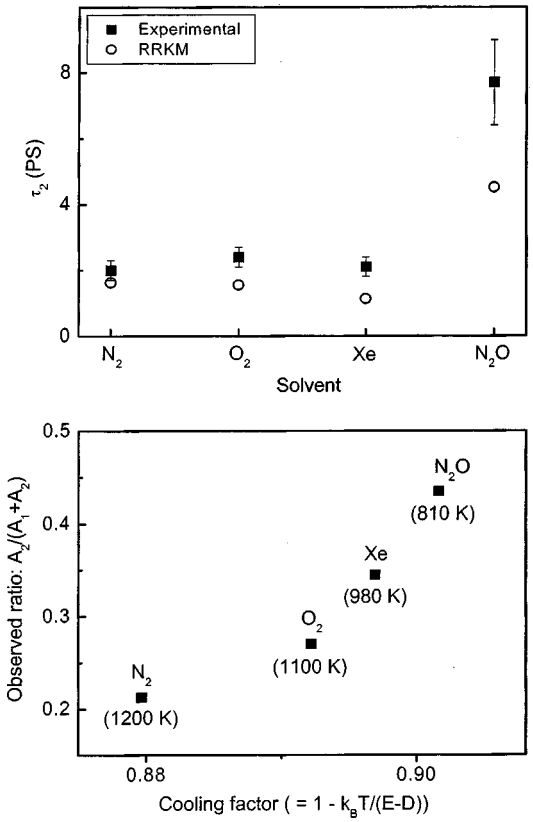

FIG. 6. Upper panel: solvent dependence of the slow time constant (τ_2): the experimental result (square) is plotted against the theoretical values (circle) estimated from the RRKM theory (see the text). Lower panel: branching ratio of the slow component, as a function of the cooling factor; the estimated temperatures are indicated (see the text).

picosecond (ps). On the lower panel, the direct (right) and indirect (left) trajectories are represented schematically in a configuration space.

When O_6^- is solvated by an additional molecule, the fast component [Eq. (1a)] slows down to approximately 200 fs, and the rate is nearly the same, regardless of the solvent molecule. This trend suggests that the fast component is not significantly influenced by the vibrational/rotational degrees of freedom and that the rate is determined by electron recombination (ER) and the kinematics of the half-collision. For dissociation on a repulsive surface, the nuclear motion is expected to occur on the time scale of 50–200 fs.[26] However, electron recombination in $O_4 \cdot O_2^-$ could occur on this time scale or longer.

For O_6^-, where electron recombination is resonant, the effective rate of electron recombination and subsequent nuclear motion is about 110 fs. The addition of the solvent, which breaks the resonance, could yield a factor of 2 lengthening of τ_1. Therefore, τ_1 is the overall time constant corresponding to ER and subsequent nuclear motion. The contribution due to kinematics appears to be insignificant in our particular systems since τ_1 does not vary with the mass of solvent X. Furthermore, Continetti and his co-workers have shown that two O_2 solvent moleclues around O_4^- act essentially as spectators in the process of O_8^- dissociative photodetachment.[27] However, as shown in the accompanying paper this kinematic effect becomes more significant as the cluster considerably increases in size.

The slow time constant (τ_2) increases by a factor of 3–10 when O_6^- is solvated. The slow time constant for $O_6^- \cdot N_2$, $O_6^- \cdot O_2$, and $O_6^- \cdot Xe$ were approximately the same ($\sim$2.0 ps), but τ_2 of $O_6^- \cdot N_2O$ was about three times longer (7.7 ps); the slow component for O_6^- gives $\tau_2 = 0.7$ ps. As described in Eq. (1b), the rate of indirect dissociation is determined by IVR, and we expect that the degree of IVR would be different for $O_6^- \cdot X$ clusters, depending on the composition (monatomic Xe; diatomic O_2 and N_2; triatomic N_2O) and binding through low-frequency modes.

To examine the role of IVR, we made calculations of τ_2 using the statistical RRKM (Rice–Ramsperger–Kassel–Marcus) theory:

$$k = \sigma \frac{N^{\ddagger}(E-D)}{h\rho(E)}, \tag{2}$$

where σ is the degeneracy in the dissociation, h is Planck's constant, $N^{\ddagger}(E-D)$ is the number of states at the transition state, and $\rho(E)$ is the density of states of the reactant at the total energy (see Ref. 28). $N^{\ddagger}(E-D)$ and $\rho(E)$ were approximated by using the intermolecular frequencies of $O_2^- \cdot X$. In other words, because the reaction coordinate on the excited potential involves $O_4O_2^- \cdot X$ we considered $O_2^- \cdot X$ for a full *ab initio* calculation and similarly for O_2^- with $2O_2$. The *ab initio* calculation was done using the unrestricted

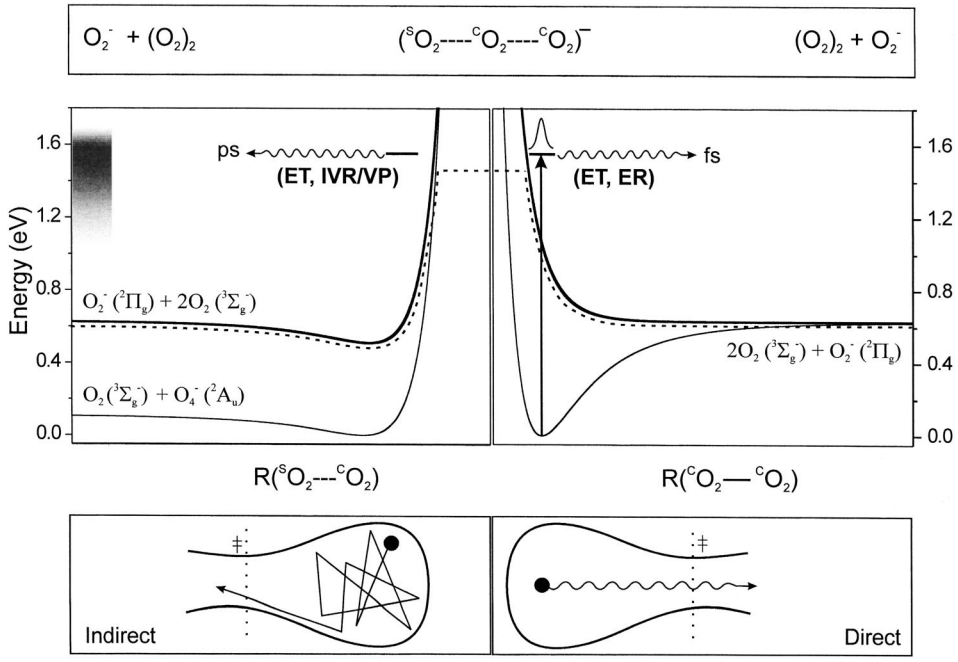

FIG. 7. Upper panel: S_N2-type reaction pathway that is shown as the dotted line in the middle panel. Middle panel: A representation of two cuts in the O_6^- potential energy surface. On the left-hand side of the figure, the potential is along the nuclear coordinate between the O_2^- and core O_4 ($^SO_2\cdots{}^CO_2$); charge-induced–dipole interaction. On the right-hand side, the potential for the separation ($^CO_2-{}^CO_2$) of O_2^- from O_2 in core O_4^- is displayed; the solvent neutral O_2 is considered as a spectator. The wave packet is prepared as indicated, and the bifurcation is illustrated by the dotted path. The estimated energy range of the charge transfer band is depicted by a shaded block on the vertical axis. Lower panel: The direct and indirect dynamics are represented schematically in the configuration space, where the horizontal axis represents the reaction coordinate while the vertical axis describes all nonreactive coordinates.

Hartree–Fock level of theory with 6-311+G^* as the basis set. E is the energy of the excitation pulse minus the difference in energy (at the minimum of the potential) between $O_2\cdot O_4^-$ and $O_2^-\cdot O_4$. We took E to be the same for all clusters, since the stabilization by X is about the same for $O_2\cdot O_4^-$ and $O_2^-\cdot O_4$.

In our calculations, three different dissociation channels were considered since all of them, shown below, can be observed in our probe window:

$$O_4^-O_2\cdot X+800\ \text{nm}\rightarrow O_4O_2^-\cdot X\xrightarrow{k_a}O_2^-+X+2O_2 \tag{3a}$$

$$\xrightarrow{k_b}O_2^-\cdot O_2+X+O_2\rightarrow O_2^-+X+2O_2 \tag{3b}$$

$$\xrightarrow{k_c}O_2^-\cdot X+2O_2\rightarrow O_2^-+X+2O_2 \tag{3c}$$

For X=N_2, Xe, or N_2O, k_a, k_b, and k_c were calculated using $\sigma=1$, 2, and 1, respectively. In the case of X=O_2, k_a and k_b were calculated using $\sigma=1$ and 3. The τ_2 values calculated by the RRKM theory correspond to the reciprocal of the total rate constant ($k_{\text{total}}=k_a+k_b+k_c$). We found that k_b and k_c are dominant, consistent with the fact that the dissociation energy for Eqs. (3b) and (3c) are smaller than that of (3a). In the case of channel (3b) and (3c), the subsequent dissociation of metastable $O_2^-\cdot X$ occurs. However, this subsequent dissociation will not appear in our transient because photoelectron signals of $O_2^-\cdot X$, as well as O_2^-, are integrated in our boxcar gate and the photodetachment cross section of O_2^- and $O_2^-\cdot X$ is about the same; the change from $O_2^-\cdot X$ to O_2^- is not sensitive enough to our probe. In all these calculations, the transition state was taken to be a product type, without variational adjustment. The results show the trend shown in Fig. 6, which parallels that of the experimental results, and the values are in Table I.

The amplitude ratio ($\gamma\equiv A_1/A_2$) varies as a function of the solvent X, which is also consistent with the solvent effect on the bifurcation process. A large γ value ($\gamma=A_1/A_2>1$) means that the direct process is more favored than the indirect one, and *vice versa*. The electron recombination (ER) is governed by the energetics of O_2^- and O_4 in the charge transferred $O_2^-\cdot O_4$ complex. The solvent effect on ER is mainly due to the dissipation of O_2^- internal energy to the solvent and the energetics. When the incipient O_2^- maintains its initial vibrational energy, electron recombination is most favored, as observed in O_6^- ($\gamma=4.0$). On the other hand, when O_2^- dissipates its internal energy to the solvent, the direct process decreases in contribution. Additionally, the energy between the HOMO of O_2^- and the LUMO of O_4 is influenced by the solvent and the gap increases as O_2^- becomes solvated. Thus, the amplitude ratio of the fast and slow component should be correlated, in part, to the degree of vibrational cooling.

A cooling factor can be defined to express the fraction of available energy that goes into the internal energy of O_2^-:

$$C=1-\frac{k_BT}{E-D_{(3A)}}, \tag{4}$$

where k_B is the Boltzmann constant, T is the temperature of the nascent O_2^- fragment estimated from Fig. 3(b), E is defined above, and $D_{(3A)}$ is the dissociation energy of channel (3a). If O_2^- is very cold, C goes to 1, and if it acquires most of the internal energy, C becomes 0. This trend is illustrated on the bottom panel of Fig. 6 in which the branching ratio of the slow channel, $A_2/(A_1+A_2)$, is plotted against the cooling factor. Among the solvents, the cooling factor of N_2O is larger than all others. The unique nature of N_2O compared to Xe, O_2, and N_2 is that $O_2^-\cdot N_2O$ can effectively exchange energy via vibration-to-vibration and rotational couplings. The essential criteria of V-V transfer are near-resonance in energy and the infrared activity of the mode involved.[29,30] Among the solvents studied, only N_2O fulfills these criteria.

V. CONCLUSION

We have investigated the solvent effect on O_6^- dissociation dynamics, and observed that the addition of one solvent (O_2, N_2, Xe, or N_2O) gives very different effects on the dynamics of the nuclear motion, whose wave packet bifurcates in two channels. These real time studies of the one-solvent dynamics provide the time scale for the distinctive processes of electron recombination and bond rupture, and vibrational predissociation—with both channels yielding O_2^-. As with kinetic energy resolution,[31] here the photoelectron resolution[5] allows us to examine the dynamics following the bifurcation[32] in these pathways to O_2^-. The manifestation of direct and indirect dissociations are clear in the change of the time scale with solvation, as the direct process is controlled by electron recombination and kinematics of the half-collision, while the indirect process involves energy redistribution. We compare the experimental findings reported here with *ab initio* and statistical rate calculations in these finite-sized ionic clusters. These elementary processes observed in small clusters are expected to evolve as the number of solvent molecules increases, and this aspect will be discussed in the accompanying paper where we studied the homogeneous solvated and mass-selected $(O_2)_n^-$, $n=3-10$.

ACKNOWLEDGMENTS

This work was supported by the National Science Foundation and the AFOSR. We wish to thank Dr. T. M. Bernhardt for helpful discussion in the initial stage of this work (Ref. 9).

[1] A. W. Castleman, Jr. and K. H. Bowen, J. Phys. Chem. **100**, 12911 (1996), and references therein.
[2] A. Sanov, T. Sanford, S. Nandi, and W. C. Lineberger, J. Chem. Phys. **111**, 664 (1999), and references therein.
[3] M. J. DeLuca, C.-C. Han, and M. A. Johnson, J. Chem. Phys. **93**, 268 (1990).
[4] C.-C. Han and M. A. Johnson, Chem. Phys. Lett. **189**, 460 (1992).
[5] B. J. Greenblatt, M. T. Zanni, and D. M. Neumark, Science **276**, 1675 (1997).
[6] L. Lehr, M. T. Zanni, C. Frischkorn, R. Weinkauf, and D. M. Neumark, Science **284**, 635 (1999).
[7] R. Li, K. A. Hanold, M. C. Garner, A. K. Luong, and R. E. Continetti, Faraday Discuss. **108**, 115 (1997).
[8] K. Hiraoka, Chem. Phys. **125**, 439 (1988).
[9] D. H. Paik, T. M. Bernhardt, N. J. Kim, and A. H. Zewail, J. Chem. Phys. **115**, 612 (2001).
[10] R. B. Gerber, A. B. McCoy, and A. García-Vela, Annu. Rev. Phys. Chem. **45**, 275 (1994), and references therein.
[11] D. M. Willberg, M. Gutmann, J. J. Breen, and A. H. Zewail, J. Chem. Phys. **96**, 198 (1992).
[12] M. Gutmann, D. M. Willberg, and A. H. Zewail, J. Chem. Phys. **97**, 8037 (1992).
[13] D. M. Willberg, M. Gutmann, E. E. Nikitin, and A. H. Zewail, Chem. Phys. Lett. **201**, 506 (1993).
[14] Q. Liu, J.-K. Wang, and A. H. Zewail, Nature (London) **364**, 427 (1993).
[15] B. Ernstberger, H. Krause, A. Kiermeier, and H. J. Neusser, J. Chem. Phys. **92**, 5285 (1990).
[16] P. Kruit and F. H. Read, J. Phys. E **16**, 313 (1983).
[17] W. C. Wiley and I. H. McLaren, Rev. Sci. Instrum. **26**, 1150 (1955).
[18] R. Weinkauf, K. Walter, C. Weickhardt, U. Boesl, and E. W. Schlag, Z. Naturforsch. **44a**, 1219 (1989).
[19] N. J. Kim, D. H. Paik, and A. H. Zewail, J. Chem. Phys. **118**, 6930 (2002).
[20] A. G. Khrapak and K. F. Volykhin, J. Exp. Theor. Phys. **88**, 320 (1999).
[21] L. H. Scharpen, J. S. Muenter, and V. W. Laurie, J. Chem. Phys. **53**, 2513 (1970).
[22] A. D. Buckingham, C. Graham, and J. H. Williams, Mol. Phys. **49**, 703 (1983).
[23] "Atomic and molecular polarizabilities," in *CRC Handbook of Chemistry and Physics*, 82nd ed., edited by D. R. Lide (CRC, Boca Raton, FL, 2001), p. 10–165.
[24] D. Spence and G. J. Schulz, Phys. Rev. A **2**, 1802 (1970).
[25] S. Matejcik, P. Stampfli, A. Stamatovic, P. Scheier, and T. D. Märk, J. Chem. Phys. **111**, 3548 (1999).
[26] A. H. Zewail, J. Phys. Chem. A **104**, 5660 (2000).
[27] T. G. Clements and R. E. Continetti, Phys. Rev. Lett. **89**, 033005 (2002).
[28] T. Bear and W. L. Hase, in *Unimolecular Reaction Dynamics: Theory and Experiments* (Oxford University Press, New York, 1996).
[29] J. A. Mack, K. Mikulecky, and A. M. Wodtke, J. Chem. Phys. **105**, 4105 (1996).
[30] M. Silva, R. Johgma, R. W. Field, and A. M. Wodtke, Annu. Rev. Phys. Chem. **52**, 811 (2001).
[31] D. Zhong, T. M. Bernhardt, and A. H. Zewail, J. Phys. Chem. A **103**, 10093 (1999), and references therein.
[32] K. B. Møller and A. H. Zewail, in *Essays in Contemporary Chemistry: From Molecular Structure Towards Biology*, edited by G. Quinkert and M. V. Kisakürek (Verlag Helvetica Chimica Acta, Zurich, 2001), pp. 157–188.